




Real-Time Microwave Imaging of a Compressed Breast Phantom With Planar Scanning

Daniel Tajik , *Student Member, IEEE*, Farzad Foroutan, *Student Member, IEEE*,
Denys S. Shumakov , *Member, IEEE*, Aaron D. Pitcher, *Student Member, IEEE*,
and Natalia K. Nikolova , *Fellow, IEEE*

Abstract—Two real-time reconstruction algorithms, i.e., quantitative microwave holography and scattered-power mapping, have been shown to be successful in the imaging of compressed tissue of relatively small thicknesses such as 1 and 2 cm. In both cases, planar data acquisition of frequency-swept transmission coefficients has been employed. Despite the fact that these algorithms are based on a linear forward model of scattering, they have been capable of providing quantitative estimates of the tissue permittivity due to the experimentally derived kernel of the scattering integral. Here, we demonstrate similar performance with a thicker (approximately 5 cm) compressed-breast phantom. This thickness is greater than or comparable to the median thickness employed in mammography, depending on the view (craniocaudal or mediolateral oblique). The two methods are described in a common mathematical framework for the first time. The importance of the system calibration and the choice of a host medium are discussed through experiments. A new method for focusing onto suspect regions is demonstrated. The limitations of real-time imaging are highlighted, along with an outlook to improve the image resolution and suppressing artifacts without sacrificing the reconstruction speed. Future work aims at validation with high complexity, realistic compressed-breast phantoms.

Index Terms—Microwave imaging, quantitative microwave holography, scattered power mapping, direct inversion, tissue imaging.

I. INTRODUCTION

MICROWAVE imaging has been successful in a variety of applications dealing with optically obscured targets such as concealed-weapon detection, through-the-wall imaging, non-destructive testing, meteorology, and ground-penetrating radar [1]–[7], where numerous commercial systems are in use. It also shows potential in medical diagnostics due to the nonionizing radiation, the relatively low cost and the compact light-weight

electronics [8]–[10]. Despite its advantages, microwave systems have not yet become clinical imaging tools. There are a few challenges [11] that need to be overcome to make the technology competitive with the existing imaging modalities. In the case of breast-cancer screening, the common modality is mammography. While the above advantages hold in comparison with mammography, microwave technology is yet to demonstrate comparable or better sensitivity and specificity.

The main challenge stems from the complexities of the microwave scattering in tissue, which involves high attenuation, multiple reflections as well as diffraction and refraction within a heterogeneous medium that contains both electrically large and small anatomical details along with widely varying permittivity and conductivity values; see, e.g., [12]. As a result, microwave propagation in tissue is complicated and it is intrinsically nonlinear with respect to the permittivity of the object under test (OUT). The microwave-imaging community has developed various reconstruction algorithms to handle these complexities [8]–[11], [13], [14].

Here, we focus on two recently proposed direct-inversion methods, quantitative microwave holography (QMH) [15] and scattered-power mapping (SPM) [16]. They have been shown to reconstruct the complex permittivity of tissue objects of relatively small thickness (1 to 2 cm). As other direct-inversion methods, both QMH and SPM rely on a linearizing approximation in the forward model of scattering using either Born's approximation (BA) or Rytov's approximation (RA) [5], [13], [17]–[20]. The advantage of the direct-inversion methods is that they enable real-time imaging.

Until recently, it was believed that direct inversion can produce only qualitative images [6]. However, the work in [15], [16] along with earlier work reported in [21]–[24] demonstrates that quantitative permittivity estimates of tissue objects can be obtained with methods such as QMH and SPM.

The key to quantitative reconstruction with direct-inversion methods is a calibration measurement of the system point-spread function (PSF) [5]. The measured PSF brings two important advantages. Firstly, it provides a properly scaled forward model, which enables the quantitative reconstruction. Also, this forward model is inherently system-specific thus obviating the need to approximate Green's function and the incident field with analytical or simulated field distributions. Such approximations are inadequate in the near-field measurements of tissue and they lead to model inaccuracy and image artifacts. Secondly, the

Manuscript received November 30, 2017; revised March 14, 2018; accepted May 19, 2018. Date of publication May 28, 2018; date of current version August 22, 2018. This paper was presented at the 2017 IEEE International Symposium on Antennas and Propagation and USNC-URSI Radio Science Meeting, San Diego, CA, USA, Jul. 9–15, 2017. (*Corresponding author: Daniel Tajik.*)

D. Tajik, F. Foroutan, A. D. Pitcher, and N. K. Nikolova are with the Department of Electrical and Computer Engineering, McMaster University, Hamilton, ON L8S4L8, Canada (e-mail: tajikd@mcmaster.ca; foroutf@mcmaster.ca; pitchea@mcmaster.ca; nikolova@ieee.org).

D. S. Shumakov is with the Regulatory Operations and Regions Branch, Health Canada, Ottawa, ON K1A 0K9, Canada (e-mail: shumakds@mcmaster.ca).

Color versions of one or more of the figures in this paper are available online at <http://ieeexplore.ieee.org>.

Digital Object Identifier 10.1109/JERM.2018.2841380

measured PSF allows for inversion through deconvolution, which is numerically fast.

The disadvantage of direct-inversion methods, QMH and SPM included, stems from the linearization of the forward model. This leads to an inability to account for the mutual influence of closely spaced scatterers, which are common in tissue. Multiple scattering is also ignored; however, it is less significant due to the high attenuation. Thus, direct-inversion methods may produce lower-resolution images than nonlinear iterative methods such as microwave tomography [25], which do not employ linearizing approximations.

Still, the quantitative direct-inversion methods can provide a much better starting point for the nonlinear reconstruction than the commonly employed assumption of a uniform medium. Moreover, they can serve as linear-inversion modules in nonlinear reconstructions based on the Born iterative and distorted Born iterative methods [17], [26]. Therefore, quantitative direct inversion in tissue imaging is worthy of investigation in both scenarios: as stand-alone reconstruction algorithms and as linear modules within iterative reconstruction.

The aim of this work is to study the performance of QMH and SPM as stand-alone algorithms in experiments with a compressed breast-tissue phantom of realistic thickness. Compression in breast imaging reduces the signal loss through the tissue and thus improves the signal-to-noise ratio (SNR). Beside the ionizing radiation, one of the drawbacks of X-ray mammography is the level of compression which may cause pain. The mean thickness in routine mammography in a craniocaudal view is about 4.4 cm; see, for example [27]. The respective mean thickness in the mediolateral oblique view is about 4.8 cm [27]. Compression levels aiming at smaller than the above mean thicknesses are often required, leading to significant patient discomfort. It is expected that microwave-based mammography would not require uncomfortable compression since thicknesses equal to or exceeding the mean thicknesses used in X-ray mammography allow for good signal quality [11]. Here, we demonstrate imaging of breast phantoms of thickness 4.8 cm.

There is another reason that makes the investigation of the microwave imaging of the compressed breast worthwhile. It is well known that compression can exploit the significant difference in stiffness among glandular, fatty and cancerous tissues [28], [29]. Multiple measurements of the same tissue object at different compression levels displace healthy tissue more significantly than tumorous tissue. In view of the nonionizing nature of the microwave radiation, multiple measurements within a single examination session are indeed admissible, enabling better identification of cancerous regions. Before these studies can occur, QMH and SPM must be demonstrated functioning in a typical mammography breast compression scenario.

The purpose of this work is to evaluate both QMH and SPM at compression thicknesses comparable to the mean thicknesses in routine X-ray mammography. These reconstruction methods have been previously shown [15], [16] to be successful in imaging tissue phantoms, the thickness of which is about 1 cm. However, at thicknesses of approximately 5 cm, the signal-to-noise ratio (SNR) is significantly reduced due to the substantial attenuation in breast tissue. Thus, validation at mean mammography

compression is required along with strategies to deal with low data SNR.

To this end, comparisons between the Rytov and Born approximations with QMH and SPM at these thicknesses have not been done. As shown in previous work, the two approximations provide images, which may differ substantially depending on the heterogeneity of the sample and the data SNR [15]. One critical difference is that BA is sensitive to the size of high-contrast scattering objects whereas RA is not. On the other hand, the RA-based reconstruction exhibits sensitivity to sharp discontinuities in the spatial dependence of the phase of the data across the acquisition plane. Since the volume has been increased five-fold from previous tissue experiments, re-evaluation of the two approximations is necessary. To verify the approximations, a simplistic compressed-breast tissue phantom is constructed. Finally, since both QMH and SPM can execute within seconds, filtering strategies can be easily implemented and explored. In particular, here we show that focusing filters can improve the diagnostic quality of the final images.

II. FORWARD MODEL OF SCATTERING

Both QMH and SPM operate on frequency-domain responses such as S -parameters. Wide-bandwidth frequency sweeps are used as they improve the spatial resolution [5]. The forward model of scattering in terms of S -parameter data is given by [5], [30]:

$$S_{ik}^{\text{sc,OUT}}(\mathbf{r}; f) = \frac{i\omega\epsilon_0}{2a_i a_k} \iiint_V \Delta\epsilon_r(\mathbf{r}') \mathbf{E}_i^{\text{inc}}(\mathbf{r}', \mathbf{r}; f) \cdot \mathbf{E}_k^{\text{tot}}(\mathbf{r}', \mathbf{r}_{\text{Tx}}; f) dv' \quad (1)$$

where $S_{ik}^{\text{sc,OUT}}$ is the scattering portion of the S -parameter measured with the OUT, i.e., the portion due to the presence of the OUT in the background (or host) medium. Note that the S -parameters are not zero in the absence of an OUT because reflection and transmission still occur at the terminals of the transmitting (Tx) and receiving (Rx) antennas. The S -parameter is acquired at the location \mathbf{r} and at frequency f . The position inside the imaged volume V is denoted by $\mathbf{r}' = (x', y', z')$. In the case of planar scans, $\mathbf{r} \equiv (x, y, \bar{z})$, where the acquisition plane is fixed at \bar{z} and the Rx antenna scans laterally along x and y . Also, $i = \sqrt{-1}$ and a_ζ ($\zeta = i, k$) is the incoming root-power wave at the ζ antenna, when it operates in a Tx mode. Assuming all quantities are root-mean-square (RMS) phasors, a_ζ is the square root of the incoming power at the ζ -th port. Further, ϵ_0 is the permittivity of free space and

$$\Delta\epsilon_r(\mathbf{r}') = \epsilon_{r,\text{OUT}}(\mathbf{r}') - \epsilon_{r,\text{b}}(\mathbf{r}') \quad (2)$$

is the permittivity contrast in the volume of interest V . Here, $\epsilon_{r,\text{OUT}}$ and $\epsilon_{r,\text{b}}$ are the complex relative permittivities of the OUT and the background, respectively. Note that the latter is known at least approximately. $\mathbf{E}_i^{\text{inc}}(\mathbf{r}', \mathbf{r}; f)$ is the incident-field distribution as a function of $\mathbf{r}' \in V$ produced by the Rx (i -th) antenna if it were to operate in a Tx mode at the location \mathbf{r} . $\mathbf{E}_k^{\text{tot}}(\mathbf{r}', \mathbf{r}_{\text{Tx}}; f)$ is the total-field distribution as a function of \mathbf{r}' due the Tx (k -th) antenna k at \mathbf{r}_{Tx} .

In our setup, the Rx and Tx antennas are aligned along each other's boresight and move together along x and y on two parallel planes on both sides of the OUT, i.e., $\mathbf{r}_{\text{Tx}} = (x, y, \bar{z} + D)$, where D is the distance between the two planes. Thus, \mathbf{r} defines uniquely the position of both the Rx and the Tx antennas and the explicit use of \mathbf{r}_{Tx} is unnecessary.

Applying Born's approximation [17] to the total internal field

$$\mathbf{E}_k^{\text{tot}}(\mathbf{r}', \mathbf{r}; f) \approx \mathbf{E}_k^{\text{inc}}(\mathbf{r}', \mathbf{r}; f), \quad (3)$$

and substituting (3) into (1) leads to the linearized forward model of scattering:

$$S_{ik}^{\text{sc,OUT}}(\mathbf{r}; f) \approx \frac{i\omega\epsilon_0}{2a_i a_k} \iiint_V \Delta\epsilon_r(\mathbf{r}') [\mathbf{E}_i^{\text{inc}} \cdot \mathbf{E}_k^{\text{inc}}](\mathbf{r}', \mathbf{r}; f) dv'. \quad (4)$$

The incident-field dot product $[\mathbf{E}_i^{\text{inc}} \cdot \mathbf{E}_k^{\text{inc}}](\mathbf{r}', \mathbf{r}; f)$, also referred to as the resolvent kernel [21], can be acquired using the measured point-spread function (PSF). Consider the measurement of an electrically small scattering probe of known size Ω_{sp} and known relative permittivity $\epsilon_{r,\text{sp}}$ embedded in a uniform background medium at position $\mathbf{r}'_{\text{sp}} = (x'_{\text{sp}}, y'_{\text{sp}}, z'_{\text{sp}})$. The contrast function of the scattering probe can be represented as $\Delta\epsilon_r(\mathbf{r}') = \Delta\epsilon_{r,\text{sp}}\delta(\mathbf{r}' - \mathbf{r}'_{\text{sp}})$, where $\delta(\mathbf{r}')$ is the 3-D Dirac delta function. Here, $\Delta\epsilon_{r,\text{sp}} = \epsilon_{r,\text{sp}} - \epsilon_r$. Based on (4), the response of the scattering probe can now be written as

$$S_{ik}^{\text{sc,PSF}}(\mathbf{r}, \mathbf{r}'_{\text{sp}}; f) \approx \frac{i\omega\epsilon_0 \Delta\epsilon_{r,\text{sp}}(\mathbf{r}')\Omega_{\text{sp}}}{2a_i a_k} [\mathbf{E}_i^{\text{inc}} \cdot \mathbf{E}_k^{\text{inc}}](\mathbf{r}'_{\text{sp}}, \mathbf{r}; f). \quad (5)$$

This is the system PSF for a point scatterer at \mathbf{r}'_{sp} . It follows that the respective resolvent kernel is derived from the PSF as

$$[\mathbf{E}_i^{\text{inc}} \cdot \mathbf{E}_k^{\text{inc}}](\mathbf{r}'_{\text{sp}}, \mathbf{r}; f) \approx \frac{S_{ik}^{\text{sc,PSF}}(\mathbf{r}, \mathbf{r}'_{\text{sp}}; f)2a_i a_k}{i\omega\epsilon_0 \Delta\epsilon_{r,\text{sp}}(\mathbf{r}')\Omega_{\text{sp}}}. \quad (6)$$

Assuming the background is uniform, the PSF is translationally invariant in the lateral directions x and y . In other words, if the PSF is measured with the scattering probe at the center of the plane $z'_{\text{sp}} = \text{const.}$, $\mathbf{r}'_0 = (0, 0, z'_{\text{sp}})$, then the PSF can be derived for any other scattering-probe position $\mathbf{r}'_{\text{sp}} = (x'_{\text{sp}}, y'_{\text{sp}}, z'_{\text{sp}})$ as

$$\begin{aligned} S_{ik}^{\text{sc,PSF}}(x, y, \bar{z}; x'_{\text{sp}}, y'_{\text{sp}}, z'_{\text{sp}}; f) \\ = S_{ik}^{\text{sc,PSF}}(x - x'_{\text{sp}}, y - y'_{\text{sp}}, \bar{z}; 0, 0, z'_{\text{sp}}; f). \end{aligned} \quad (7)$$

Note that for each imaged z' -plane, a separate PSF measurement with the scattering probe at $z'_{\text{sp}} = z'$ is required. Analytical approximations of the z dependence of the PSF are also possible [5] but have not been employed here.

Using (6) and the PSF in (7), the forward model in (4) is expressed as

$$S_{ik}^{\text{sc,OUT}}(\mathbf{r}) \approx \iiint_V \rho(\mathbf{r}') S_{ik}^{\text{sc,PSF}}(\mathbf{r} - \mathbf{r}'_{xy}, \mathbf{r}'_0) dv' \quad (8)$$

where $\mathbf{r}'_{xy} = (x', y', 0)$, and

$$\rho(\mathbf{r}') = \Delta\epsilon_r(\mathbf{r}') \cdot (\Delta\epsilon_{r,\text{sp}}\Omega_{\text{sp}})^{-1} \quad (9)$$

is the reflectivity function to be recovered. The above integral is a 2-D convolution (in x, y) of $\rho(\mathbf{r}')$ and the PSF. Thus, both the QMH and the SPM methods essentially perform inversion

through 2-D deconvolution at each z' plane to obtain the respective slice of the OUT image. The difference between the two methods lies in the way this inversion is done.

III. APPROXIMATIONS OF THE SCATTERING DATA

The scattered responses $S_{ik}^{\text{sc,OBJ}}$ of the imaged objects (OBJ), OBJ denoting either the OUT or the PSF, cannot be measured directly.

They are derived from two measurements. The first is a calibration measurement, which is independent of the OUT. It is carried out in the background without any embedded scatterers and it provides the incident-field portion of the response S_{ik}^{inc} . The measurement with a scattering probe is also part of the system calibration and it provides the total-field PSF $S_{ik}^{\text{tot,PSF}}$. Finally, the measurement of the OUT provides the total-field OUT response $S_{ik}^{\text{tot,OUT}}$.

A. Born's Approximation

Born's approximation (BA) relies on the assumption that the total-field response is a superposition of the incident and scattered field responses [5], [19]:

$$S_{ik}^{\text{tot,OBJ}}(\mathbf{r}; f) \approx S_{ik}^{\text{inc}}(\mathbf{r}; f) + S_{ik}^{\text{sc,OBJ}}(\mathbf{r}; f), \quad (10)$$

where $S_{ik}^{\text{sc,OBJ}}(\mathbf{r})$ is the scattered field response. With this assumption, the scattered portions of the PSF and the OUT responses are derived as

$$S_{ik}^{\text{sc,OBJ}}(\mathbf{r}; f) \approx S_{ik}^{\text{tot,OBJ}}(\mathbf{r}; f) - S_{ik}^{\text{inc}}(\mathbf{r}; f). \quad (11)$$

The applicability of BA is constrained by both the size and the contrast of the OUT [5], [17]. Large, high-contrast scatterers may lead to image artifacts and degradation of the quantitative accuracy. This is important bearing in mind the relatively large thickness required to image a realistic breast phantom.

B. Rytov's Approximation

Rytov's approximation (RA) views the total-field response as a phase correction of the incident field with the complex phase being a scaled version of the scattered-field response [5], [17], [19]:

$$S_{ik}^{\text{tot,OBJ}}(\mathbf{r}; f) \approx S_{ik}^{\text{inc}}(\mathbf{r}; f) \cdot \exp\left(\frac{S_{ik}^{\text{sc,OBJ}}(\mathbf{r}; f)}{S_{ik}^{\text{inc}}(\mathbf{r}; f)}\right). \quad (12)$$

To extract the scattered component, (12) is rearranged:

$$S_{ik}^{\text{sc,OBJ}}(\mathbf{r}; f) \approx S_{ik}^{\text{inc}}(\mathbf{r}; f) \cdot \ln\left(\frac{S_{ik}^{\text{tot,OBJ}}(\mathbf{r}; f)}{S_{ik}^{\text{inc}}(\mathbf{r}; f)}\right). \quad (13)$$

Unlike BA, RA is limited only by the permittivity contrast and it is not sensitive to the size of the scattering object [5], [17]. This is an important advantage in breast imaging where the electrical size of the OUT is large but the contrast between malignant and healthy tissue is low.

One should be aware that RA is sensitive to phase wrapping, which is not a factor in BA. Consider (13) written in terms of

magnitude and phase:

$$S_{ik}^{\text{sc,OBJ}}(\mathbf{r}; f) = S_{ik}^{\text{inc}}(\mathbf{r}; f) \cdot \left\{ \ln \frac{|S_{ik}^{\text{tot,OBJ}}(\mathbf{r}; f)|}{|S_{ik}^{\text{inc}}(\mathbf{r}; f)|} + i [\angle S_{ik}^{\text{tot,OBJ}}(\mathbf{r}; f) - \angle S_{ik}^{\text{inc}}(\mathbf{r}; f)] \right\}. \quad (14)$$

The imaginary part of (14) is different depending on whether the signal is phase wrapped or unwrapped. Thus, in order to generate a valid reconstruction, it is recommended that all responses are phase unwrapped before applying RA.

IV. QUANTITATIVE MICROWAVE HOLOGRAPHY

QMH solves (8) in the Fourier domain where the 2-D convolution is replaced by a multiplication. The integration along z' is replaced by a discrete sum, leading to

$$\tilde{S}_{ik}^{\text{sc,OUT}}(\boldsymbol{\kappa}, \bar{z}; f) \approx \sum_z \tilde{\rho}(\boldsymbol{\kappa}, z') \tilde{S}_{ik}^{\text{sc,PSF}}(\boldsymbol{\kappa}, z'; f) \Omega_v. \quad (15)$$

Here, $\tilde{S}_{ik}^{\text{sc,OUT}}$, $\tilde{\rho}$, and $\tilde{S}_{ik}^{\text{sc,PSF}}$ are the respective Fourier-transformed quantities in (8), $\boldsymbol{\kappa} = (\kappa_x, \kappa_y)$ is the spectral position in the Fourier domain, and Ω_v is the volume of a voxel. It is important to note that the data acquired in tissue imaging must be normalized with respect to the signal strength in order to compensate for its strong frequency dependence, i.e., its decline with increasing frequency. This normalization procedure can be found in [15].

The reflectivity function $\tilde{\rho}(\boldsymbol{\kappa})$ is found one spectral position $\boldsymbol{\kappa}$ at a time by solving the system of equations:

$$\mathbf{A}(\boldsymbol{\kappa}) \tilde{\rho}(\boldsymbol{\kappa}) = \mathbf{b}(\boldsymbol{\kappa}) \quad (16)$$

where

$$\mathbf{A}(\boldsymbol{\kappa}) = \begin{bmatrix} \tilde{S}_{ik}^{\text{sc,PSF}}(\boldsymbol{\kappa}, z_1, f_1) & \cdots & \tilde{S}_{ik}^{\text{sc,PSF}}(\boldsymbol{\kappa}, z_{N_z}, f_1) \\ \vdots & \ddots & \vdots \\ \tilde{S}_{ik}^{\text{sc,PSF}}(\boldsymbol{\kappa}, z_1, f_{N_f}) & \cdots & \tilde{S}_{ik}^{\text{sc,PSF}}(\boldsymbol{\kappa}, z_{N_z}, f_{N_f}) \end{bmatrix} \quad (17)$$

$$\tilde{\rho}(\boldsymbol{\kappa}) = \Omega_v [\tilde{\rho}(\boldsymbol{\kappa}, z_1) \cdots \tilde{\rho}(\boldsymbol{\kappa}, z_{N_z})]^T \quad (18)$$

$$\mathbf{b}(\boldsymbol{\kappa}) = [\tilde{S}_{ik}^{\text{sc,OUT}}(\boldsymbol{\kappa}, f_1) \cdots \tilde{S}_{ik}^{\text{sc,OUT}}(\boldsymbol{\kappa}, f_{N_f})]^T. \quad (19)$$

Here, z'_m , $m = 1, \dots, N_z$, is the depth position and f_n , $n = 1, \dots, N_f$, is the frequency sample. The system is typically solved using the pseudoinverse function due to the rectangular structure of $\mathbf{A}(\boldsymbol{\kappa})$ [15].

Once the reflectivity function at each depth position z' is found in the 2-D Fourier domain, inverse 2-D Fourier transform is applied to obtain its distribution in real space as a function of x' and y' . The relative permittivity distribution of the OUT is derived from the reflectivity function as

$$\epsilon_{r,\text{OUT}}(\mathbf{r}') \approx \Delta \epsilon_{r,\text{sp}} \Omega_{\text{sp}} \Omega_v^{-1} \cdot \rho(\mathbf{r}') + \epsilon_{r,b}. \quad (20)$$

As shown in [21], the approximate forward model in (4) improves if either of the following requirements are fulfilled

$$\epsilon_{r,\text{OUT}}(\mathbf{r}') \approx \epsilon_{r,\text{sp}} \quad (21)$$

or

$$|\epsilon_{r,\text{OUT}}(\mathbf{r}')|, |\epsilon_{r,\text{sp}}| \ll |\epsilon_{r,b}|. \quad (22)$$

In tissue imaging, achieving (21) is not feasible since the permittivity in breast tissues can vary widely. However, the background permittivity can be selected to be higher in absolute value than that of both the scattering probe and the inspected tissue object, satisfying (22). Increasing $|\epsilon_{r,b}|$ through increased loss of the background medium is beneficial in reducing reflections from enclosures and other components of the measurement setup. However, compromise must be made between increasing the losses in the background medium and the SNR of the data. Finally, selecting $\epsilon_{r,\text{sp}}$ to be similar to the permittivity of a particular tissue target (e.g., cancer) improves the quantitative result for this target in the image.

V. SCATTERED POWER MAPPING

The SPM algorithm starts by constructing the scattered-power map of the OUT at each frequency. These are 3-D complex-valued maps, which are in essence qualitative images of the OUT complex contrast [5], [16]. They are expressed as

$$M_{ik}^{\text{OUT}}(\mathbf{r}'; f) = \iint_{xy} S_{ik}^{\text{sc,OUT}}(\mathbf{r}; f) \cdot [S_{ik}^{\text{sc,PSF}}(\mathbf{r}; \mathbf{r}'; f)]^* dx dy \quad (23)$$

where the asterisk denotes conjugation, $\mathbf{r} = (x, y, \bar{z})$, and $\mathbf{r}' = (x', y', z')$. Substituting (8) into (23) and exchanging the order of integration leads to

$$M_{ik}^{\text{OUT}}(\mathbf{r}'; f) \approx \iiint_{x' y' z'} \rho(\mathbf{r}'') \cdot M_{ik}^{\text{PSF}}(\mathbf{r}'; \mathbf{r}''; f) dx'' dy'' dz'' \quad (24)$$

where $\mathbf{r}'' = (x'', y'', z'')$, and

$$M_{ik}^{\text{PSF}}(\mathbf{r}'; \mathbf{r}''; f) = \iint_{xy} S_{ik}^{\text{sc,PSF}}(\mathbf{r}; \mathbf{r}''; f) \cdot [S_{ik}^{\text{sc,PSF}}(\mathbf{r}; \mathbf{r}'; f)]^* dx dy \quad (25)$$

is the 3-D scattered-power map as a function of \mathbf{r}' (i.e., the qualitative image) of the scattering probe when it is positioned at \mathbf{r}'' . In the case of uniform background, the PSF power maps are translationally invariant in x and y , which allows (24) to be written in terms of a 2-D convolution similarly to (8):

$$M_{ik}^{\text{OUT}}(\mathbf{r}'; f) \approx \iiint_{x' y' z'} \rho(\mathbf{r}'') \cdot M_{ik}^{\text{PSF}}(\mathbf{r}' - \mathbf{r}''_{xy}; \mathbf{r}''_0; f) dx'' dy'' dz'' \quad (26)$$

where $\mathbf{r}''_{xy} = (x'', y'', 0)$ and $\mathbf{r}''_0 = (0, 0, z'')$.

With multi-frequency data, $\mathbf{M}_{ik}^{\text{OUT}}$ and $\mathbf{M}_{ik}^{\text{PSF}}$ are combined into a single map [16], [21]:

$$M^{\text{OBJ}}(\mathbf{r}') = \frac{1}{N_f} \sum_{m=1}^{N_f} \frac{M_{ik}^{\text{OBJ}}(\mathbf{r}', f_m)}{\max(|M_{ik}^{\text{PSF}}(\mathbf{r}'; \mathbf{r}''_0; f_m)|)} \quad (27)$$

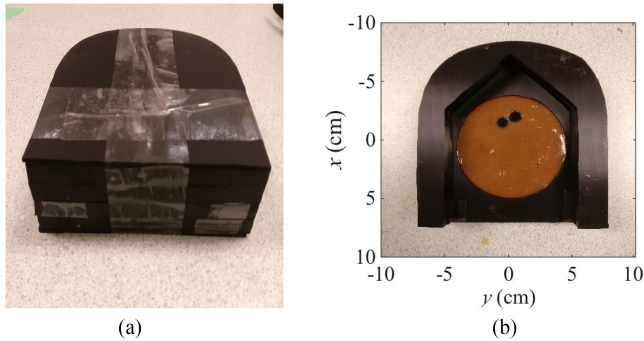


Fig. 1. Compressed breast phantom. (a) Fully constructed phantom approximately 4.8 cm thick and (b) partially constructed phantom showing the location of the blueberries, 2 cm above the base of the phantom.

where $\text{OBJ} \equiv \text{OUT}$, PSF. The above linear combination of scattered-power maps can be extended to include the S -parameters for all Rx and Tx antennas, indexed by i and k , respectively. Since the linear combination of (27) is applied to both the left side of (26) and to its kernel, the forward model of the SPM can be finally stated as

$$M^{\text{OUT}}(\mathbf{r}') \approx \iiint_{x'' y'' z''} \rho(\mathbf{r}'') \cdot M^{\text{PSF}}(\mathbf{r}' - \mathbf{r}''_{xy}; \mathbf{r}'_0) dx'' dy'' dz''. \quad (28)$$

Similarly to QMH, we cast (28) into 2-D Fourier domain as

$$\widetilde{M}^{\text{OUT}}(\boldsymbol{\kappa}, z') \approx \Omega_v \sum_{z''} \widetilde{\rho}(\boldsymbol{\kappa}, z'') \widetilde{M}_{\mathbf{r}'_0}^{\text{PSF}}(\boldsymbol{\kappa}, z') \quad (29)$$

where $\widetilde{M}_{\mathbf{r}'_0}^{\text{PSF}}(\boldsymbol{\kappa}, z')$ is the 2-D Fourier transform of $M^{\text{PSF}}(\mathbf{r}'; \mathbf{r}'_0)$ with respect to x' and y' . Thus, the reflectivity $\widetilde{\rho}(\boldsymbol{\kappa}, z'')$ is recovered by solving a linear system of equations at each spectral position $\boldsymbol{\kappa}$, similarly to (15). The difference is that here the system matrix is of size $N_z \times N_z$ whereas the QMH system matrix is of size $N_f \times N_z$. In either case, these linear systems of equations are very small and their solution is found practically instantaneously. In our experiments, N_f is typically on the order of 10 to 100, whereas N_z is on the order of 3 to 10.

VI. COMPRESSED BREAST PHANTOM EXPERIMENT

A. Acquisition Setup

QMH and SPM have been previously used to image thin tissue phantoms approximately 1 cm thick [16], [24], [31]. To ensure these methods are clinically viable, they are tested here with tissue thickness similar to that in mammography.

We have constructed a 4.8 cm thick modifiable compressed breast phantom; see Fig. 1. The permittivities of all phantom components were measured from 3 GHz to 8 GHz using a slim form probe [32]. Their averages are shown in Table I.

The bulk of the phantom is comprised of four 1.1 cm thick stacked carbon-rubber sheets custom-ordered from Emerson & Cuming Ltd. (now Laird Tech). These sheets are carefully designed to have a permittivity and loss similar to that of averaged scattered fibroglandular (Class-2) breast tissue [33]. They were cut to form the shape of a compressed breast. A house-shaped

TABLE I
AVERAGED DIELECTRIC PROPERTIES OF MATERIALS FROM 3 GHz TO 8 GHz

Material (Structure)	ϵ'	ϵ''
Thick Carbon-rubber Sheet (Averaged Breast Tissue)	10.91	2.84
PBJ (Embedding Medium)	10.41	5.07
Thin Carbon-rubber Sheet (Averaged Skin Tissue)	15.69	10.28
Blueberry (Cancerous Tissue)	55.27	16.63
Scattering Probe (PSF)	50.00	0.05

section from each carbon-rubber sheet is separated to provide flexibility inserting different contrast structures into different layers of the phantom. The second layer from the bottom has a circular section removed and a Petri dish is inserted containing two blueberries. Since blueberries have similar permittivity to that of cancerous breast tissue [11], [34], they are used to emulate a small cancerous structure within the breast. The blueberries are surrounded with a peanut butter and jam mixture (PBJ) which is designed to have similar permittivity to the carbon-rubber sheets. To construct the PBJ, a 9:1 jam to peanut butter volume ratio was mixed together in a food blender. The ratio of PBJ was determined by mixing different quantities and repeatedly measuring with an Agilent slim form probe [32] until the correct permittivity was acquired. Using PBJ as an embedding medium removes air gaps with high permittivity contrast that could violate the limitations of both BA and RA. High permittivity contrast with air gaps has been shown in previous work to severely hinder the quantitative reconstruction [16], [24]. On both the top and bottom of the phantom, a 2 mm thick carbon-rubber sheet of a higher relative permittivity (JCS-15, Laird Tech) than the thick sheets (see Table I) was placed to represent skin. Finally, the phantom is wrapped in thin plastic wrap. Overall, this phantom represents a simplified compressed breast and is the first stage towards experimenting with thicker, more complex phantoms.

The OUT is the compressed breast phantom placed in a 30 cm by 30 cm *Plexiglas* tray and surrounded with a background medium made of PBJ identical to the mixture surrounding the blueberries. An image of the blueberry layer is shown in Fig. 1(b). The OUT is completed with a *Plexiglas* lid of the same thickness as the base of the tray. The PSF measurement is that of a small dielectric cylinder ($\epsilon_r \approx 50 - 0i$, radius = 0.5 cm, height = 1.0 cm) inserted in the PBJ medium at the center of the tray and aligned at the same range location as that of the Petri-dish layer of the phantom. The incident-field measurement is that of the tray containing the PBJ medium.

The acquisition setup comprises two transverse electromagnetic (TEM) horns impedance matched to the carbon-rubber sheets [35]. The horns are aligned along boresight and are positioned approximately 2 mm away from the top and bottom *Plexiglas* plates, which are 4 mm thick. The overall distance between the apertures of the two antennas is 6 cm. The setup is shown in Fig. 2.

A raster scan is performed across a 20 cm by 20 cm acquisition area at 2 mm increments following the guidelines suggested in [15]. Transmission data S_{21} is acquired in a frequency bandwidth from 3 GHz to 8 GHz at 100 MHz intervals, generating

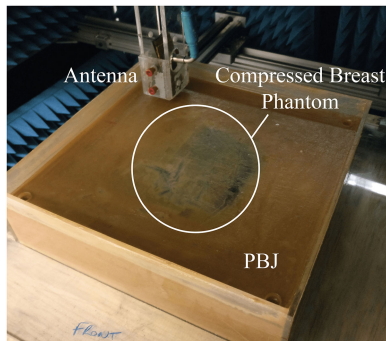


Fig. 2. Acquisition setup during the OUT measurement. A lid is placed over the compressed breast phantom which is centered in the PBJ mixture. The antennas are positioned 2 mm above and below the *Plexiglas* plates.

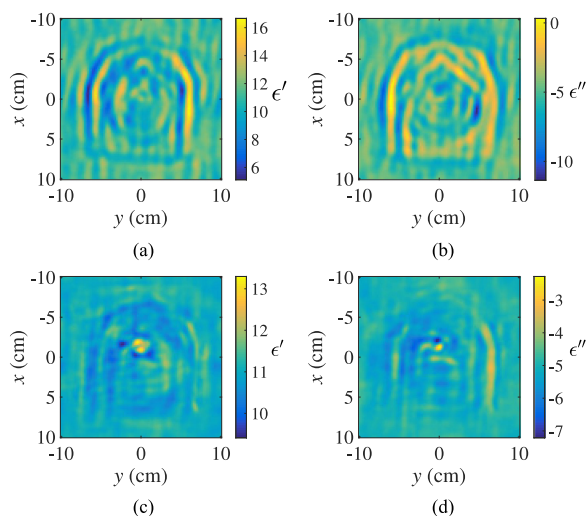


Fig. 3. Reconstructed images of the compressed breast phantom using QMH (permittivity relative to vacuum). (a) Real permittivity with BA, (b) imaginary permittivity with BA, (c) real permittivity with RA, and (d) imaginary permittivity with RA.

over 600 000 individual data points. A 3-W continuous-wave power amplifier [36] is attached to the Tx antenna, and a 35 dB low-noise amplifier [37] is attached at the Rx antenna.

The mechanical scan is slow. In this case, it takes close to 6 hours. It is clear that while the current prototype offers flexibility in optimizing the acquisition setup and the sampling step, it cannot be used in the clinic. An electronically switched system is currently under development [38]–[40], which is estimated to complete a full scan in about 2 minutes.

B. Results

The reconstructed images using QMH and SPM are shown in Figs. 3 and 4. The computation takes 1.5 seconds using MATLAB on a 2013 Macbook Pro. Qualitatively, QMH and SPM produce similar results when using the same scattered-data approximation (BA or RA). In the BA reconstruction, the contours of the breast phantom appear strongly. This is due to air pockets which reside along the edges of the phantom. The air pockets present large high-contrast structures that impact the inversion

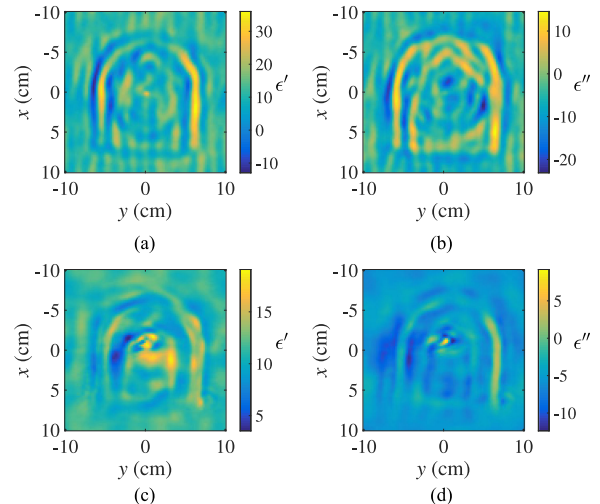


Fig. 4. Reconstructed images of the compressed breast phantom using SPM (permittivity relative to vacuum). (a) Real permittivity with BA, (b) imaginary permittivity with BA, (c) real permittivity with RA, and (d) imaginary permittivity with RA.

negatively. This makes the blueberries, located approximately around (0, 0), difficult to discern.

On the other hand, QMH and SPM under RA successfully locate the blueberries. This is due to the insensitivity of RA to the size of the scattering objects. However, RA is unable to accurately depict the shape of the structures.

In quantitative terms, both QMH and SPM struggle with the reconstruction. Nonphysical permittivity values ($\text{Re}\{\epsilon_r\} < 1$, $\text{Im}\{\epsilon_r\} > 0$) remain a significant challenge, since they cannot be submitted to an iterative solver. A simple strategy for removing nonphysical values has already been proposed in [41].

VII. DISCUSSION

A. Permittivity of the Background Medium

It was shown in [21] that a background permittivity larger than the OUT permittivity improves the accuracy of the linearized forward model when using a PSF-based kernel. Also, since the PBJ is very lossy, reflections due to the acquisition setup are suppressed. These reflections have been shown to often corrupt the image reconstruction [15]. For clinical studies, a medium which provides a uniform high permittivity background should be used.

B. Apodization and Fourier-Domain Filtering

Two filters, the apodization filter and the Fourier-domain low-pass filter, are used to improve the image quality in both QMH and SPM. These filters are necessary due to the methods' susceptibility to mathematical errors stemming from the use of the Fourier and inverse Fourier transform [15]. The apodization filter is a spatial window that is applied to the scattered signals of the PSF and the OUT. This filter tapers the edges of the image to zero, which avoids numerical artifacts due to discontinuous boundaries. A cosine window is selected due to its simple implementation and is illustrated in Fig. 5(a).

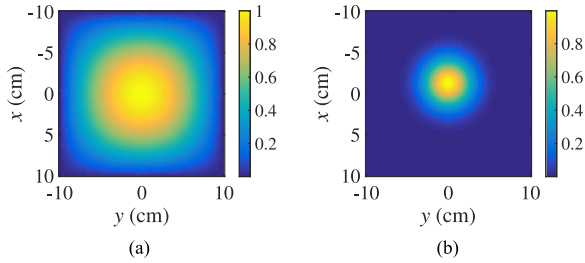


Fig. 5. Images of the apodization filters. (a) Unfocused apodization filter using a 2-D cosine function and (b) focused apodization filter using a Gaussian function centered on the blueberry location predicted by the RA reconstruction.

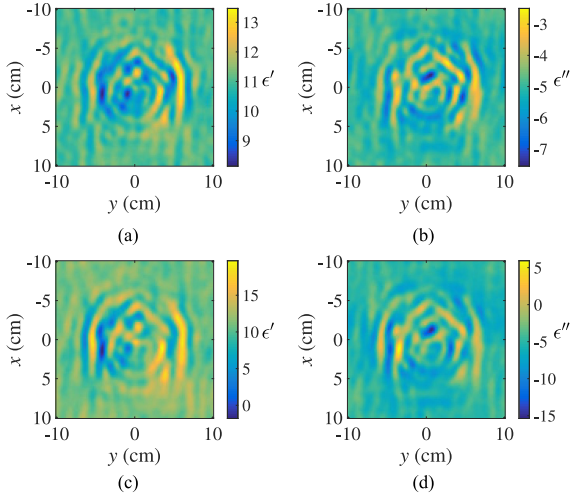


Fig. 6. Reconstructed images of the compressed breast phantom under BA and using a focusing filter (permittivity relative to vacuum). (a) Real permittivity with QMH, (b) imaginary permittivity with QMH, (c) real permittivity with SPM, and (d) imaginary permittivity with SPM.

The post-inversion low-pass filter is used to filter out the high spatial-frequency components of the Fourier transform of the reflectivity function. It is well known that a Fourier domain low-pass filter has tradeoffs between high image resolution and suppression of noise. The method used to determine the filter parameters is shown in [15].

C. Born's Approximation and Rytov's Approximation

As shown in Section VI-B, there are trade-offs in using either BA or RA to estimate the scattered data from the total-field and incident-field measurements. BA struggles with large tissue phantoms due to limitations related to size, which is not the case for RA. On the other hand, RA is prone to phase errors and it may fail to correctly identify the shape of the inclusions. There is therefore an advantage to using the RA-based reconstruction to first find regions of interest (ROI). Then, with a focused apodization filter, the BA reconstruction can successfully reconstruct details within the ROI.

Fig. 6 depicts the QMH and SPM reconstruction under BA with the focused Gaussian filter shown in Fig. 5(b). The blueberries' shape and location are reconstructed in both the real and imaginary part of the permittivity distribution obtained with both QMH and SPM.

Note that there is flexibility in the design of the focusing filter. Since both SPM and QMH execute quickly, tuning of the focusing filter can be accomplished in real time. This is a practical tool to enhance diagnostic quality.

VIII. CONCLUSION

For the first time, quantitative microwave holography (QMH) and scattered power mapping (SPM) are demonstrated as methods capable of imaging compressed dense breast tissue for cancer detection. They are shown detecting cancerous simulants in an experiment with a phantom of 4.8 cm thickness similar to the mean thickness of compressed breast in routine mammography. Two blueberries 1 cm in diameter are inserted into the breast phantom. They have permittivity similar to that of breast-cancer samples. The phantom is embedded in a high-permittivity/high-loss medium which improves the quality of the reconstruction while also suppressing unwanted reflections generated by the acquisition setup. The results demonstrate that while QMH and SPM reconstruct similar images, their implementation with either Born's approximation (BA) or Rytov's approximation (RA) has an impact on the overall reconstruction. Importantly, the RA-based reconstruction can be used to locate small scattering structures, which can then be resolved better by BA reconstruction that employs a controlled apodization filter. The QMH and SPM algorithms utilizing either BA or RA execute in MATLAB [42] within a couple of seconds on a 2013 Macbook Pro.

One critical concern with microwave imaging technology is its compliance with health and safety regulations. Due to the fact that microwave-imaging technology is still in a pre-clinical stage of development, no specific regulations exist at this time. This is in contrast with magnetic resonance imaging (MRI) technology, for which regulations exist; see, e.g., Health Canada Safety Code 26 [43]. In the meantime, the general regulations pertaining to electromagnetic radiation (typically that of communication devices), such as Health Canada Safety Code 6 [44], can be used as a reference.

Due to the very long exposure time, a mechanical scan using a 3-W transmission would not satisfy the Health Canada Safety Code 6 limitations for the specific absorption rate (SAR); see section 2.1.2 in [44]. As an example, at frequencies up to 6 GHz, the SAR basic restrictions are: 1.6 W/kg (uncontrolled environment) and 8 W/kg (controlled environment) averaged over any 6 minute reference period.¹

However, an electronically switched acquisition within 2 minutes can easily satisfy the safety regulations for a *controlled environment* with a power-transmission level of 3 W. For a 20 cm by 20 cm acquisition aperture, a two-minute measurement at 3 W input power would generate an averaged incident power density of 25 W/m², where the averaging is done over the prescribed period of 6 minutes. It was shown in a microwave breast-imaging SAR study [45] that a power density of 10 W/m² produced a peak SAR of 1.7 W/kg in the breast. Since power density and SAR are linearly related, the estimated peak SAR for our sys-

¹A controlled environment is the one which 1) has adequately characterized the RF fields intensities in the area, 2) exposure is incurred by persons who are aware and cognizant of RF exposure and intensity, and 3) exposure is incurred by persons who are aware of risks and can apply mitigation strategies [44].

tem is 4.25 W/kg, which falls well within the safety limits for a controlled environment.

Future work aims towards reconstructing 3-D images of tissue in real time. In principle, this requires PSFs for each imaged z -plane, which implies multiple PSF measurements and, therefore, increased system-calibration effort. The development of a range-translation algorithm that can synthetically shift an already measured PSF to other locations along range would eliminate the need for multiple PSF measurements.

Further study on readily available low-cost background mediums (e.g. ultrasound gel) is also necessary. To further validate the methods, more complex phantoms containing larger heterogeneities need to be imaged.

Finally, the two methods must be integrated in an iterative solver, which would improve the resolution and eliminate non-physical values. This would pave the way towards clinically-viable microwave imaging tools for breast-cancer screening.

REFERENCES

- [1] D. M. Sheen, D. L. McMakin, and T. E. Hall, "Three-dimensional millimeter-wave imaging for concealed weapon detection," *IEEE Trans. Microw. Theory Techn.*, vol. 49, no. 9, pp. 1581–1592, Sep. 2001.
- [2] M. G. Amin, *Through-the-wall Radar Imaging*. Boca Raton, FL, USA: CRC, 2016.
- [3] W. F. Hirschfeld, "The invention of radar meteorology," *Bulletin Amer. Meteorol. Soc.*, vol. 67, no. 1, pp. 33–37, Jan. 1986.
- [4] D. J. Daniels, *Ground Penetrating Radar*. Hoboken, NJ, USA: Wiley, 2005.
- [5] N. K. Nikolova, *Introduction to Microwave Imaging*. Cambridge, U.K: Cambridge Univ. Press, 2017.
- [6] M. Pastorino, *Microwave Imaging*. Hoboken, NJ, USA: Wiley, 2010.
- [7] S. Kharkovsky and R. Zoughi, "Microwave and millimeter wave nondestructive testing and evaluation—Overview and recent advances," *IEEE Instrum. Meas. Mag.*, vol. 10, no. 2, pp. 26–38, Apr. 2007.
- [8] N. K. Nikolova, *Microwave Biomedical Imaging*. Hoboken, NJ, USA: Wiley, pp. 1–22, Apr. 2014.
- [9] R. C. Conceição, J. J. Mohr, and M. O'Halloran, Eds., *An Introduction to Microwave Imaging for Breast Cancer Detection*. New York, NY, USA: Springer, 2016.
- [10] S. Kwon and S. Lee, "Recent advances in microwave imaging for breast cancer detection," *Int. J. Biomed. Imag.*, vol. 2016, 2016, Art. no. 5054912.
- [11] N. K. Nikolova, "Microwave imaging for breast cancer," *IEEE Microw. Mag.*, vol. 12, no. 2, pp. 78–94, Dec. 2011.
- [12] T. Sugitani *et al.*, "Complex permittivities of breast tumor tissues obtained from cancer surgeries," *Appl. Phys. Lett.*, vol. 104, Jun. 2014, Art. no. 253702.
- [13] A. C. Kak and M. Slaney, *Principles of Computerized Tomographic Imaging*. Piscataway, NJ, USA: IEEE Press, 1988.
- [14] K. D. Paulsen, P. M. Meaney, and L. C. Gilman, *Alternative Breast Imaging: Four Model-Based Approaches*. New York, NY, USA: Springer, 2004.
- [15] D. Tajik, A. D. Pitcher, and N. K. Nikolova, "Comparative study of the Rytov and Born approximations in quantitative microwave holography," *Prog. Electromagn. B.*, vol. 79, pp. 1–19, 2017.
- [16] D. S. Shumakov and N. K. Nikolova, "Fast quantitative microwave imaging with scattered power maps," *IEEE Trans. Microw. Theory Techn.*, vol. 66, no. 1, pp. 439–449, Jan. 2018.
- [17] W. Chew, *Waves and Fields in Inhomogeneous Media*. Piscataway, NJ, USA: IEEE Press, 1995.
- [18] J. Li, X. Wang, and T. Wang, "On the validity of Born approximation," *Prog. Electromagn. Res.*, vol. 107, pp. 219–237, 2010.
- [19] T. M. Habashy, R. W. Groom, and B. R. spies, "Beyond the Born and Rytov approximations: A nonlinear approach to electromagnetic scattering," *J. Geophys. Res.*, vol. 98, no. B2, pp. 1759–1775, Feb. 1993.
- [20] M. Slaney, A. C. Kak, and L. E. Larsen, "Limitations of imaging with first-order diffraction tomography," *IEEE Trans. Microw. Theory Techn.*, vol. MIT-32, no. 8, pp. 860–874, Aug. 1984.
- [21] S. Tu, J. J. McCombe, D. S. Shumakov, and N. K. Nikolova, "Fast quantitative microwave imaging with resolvent kernel extracted from measurements," *Inverse Probl.*, vol. 31, no. 4, 2015, Art. no. 045007.
- [22] D. S. Shumakov, S. Tu, and N. K. Nikolova, "Fast quantitative microwave imaging based on measured point spread functions and inversion in real space," in *Proc. IEEE Int. Symp. Antennas Propag./USNC/URSI Nat. Radio Sci. Meet.*, Vancouver, BC, Canada, Jul. 2015, pp. 687–688.
- [23] D. Tajik, J. R. Thompson, A. S. Beaverstone, and N. K. Nikolova, "Real-time quantitative reconstruction based on microwave holography," in *Proc. IEEE Int. Symp. Antennas Propag.*, Fajardo, PR, USA, 2016, pp. 851–852.
- [24] D. Tajik, D. S. Shumakov, and N. K. Nikolova, "An experimental comparison between the Born and Rytov approximations in microwave tissue imaging," in *Proc. IEEE MTT-S Int. Microw. Symp.*, Honolulu, HI, USA, Jun. 2017, pp. 1391–1393.
- [25] T. M. Grzegorzczak, P. M. Meaney, P. A. Kaufman, R. M. diFlorio-Alexander, and K. D. Paulsen, "Fast 3-D tomographic microwave imaging for breast cancer detection," *IEEE Trans. Med. Imag.*, vol. 31, no. 8, pp. 1584–1592, Aug. 2012.
- [26] W. C. Chew and Y. M. Wang, "Reconstruction of two-dimensional permittivity distribution using the distorted Born iterative method," *IEEE Trans. Med. Imag.*, vol. 9, no. 2, pp. 218–225, Jun. 1990.
- [27] M. A. Helvie, H.-P. Chan, D. D. Adler, and P. G. Boyd, "Breast thickness in routine mammograms: Effect on image quality and radiation dose," *Amer. J. Roentgenol.*, vol. 163, no. 6, pp. 1371–1374, Dec. 1994.
- [28] T. A. Krouskop, T. M. Wheeler, F. Kallel, B. S. Garra, and T. Hall, "Elastic moduli of breast and prostate tissues under compression," *Ultrason. Imag.*, vol. 20, no. 4, pp. 260–274, 1998.
- [29] P. Wellman, R. H. Howe, E. Dalton, and K. A. Kern, "Breast tissue stiffness in compression is correlated to histological diagnosis," Harvard BioRobotics Lab., Division Eng. Appl. Sci., Harvard Univ., Cambridge, MA, USA, Tech. Rep., 1999.
- [30] A. S. Beaverstone, D. S. Shumakov, and N. K. Nikolova, "Frequency-domain integral equations of scattering for complex scalar responses," *IEEE Trans. Microw. Theory Techn.*, vol. 65, no. 4, pp. 1120–1132, Apr. 2016.
- [31] D. S. Shumakov, D. Tajik, A. S. Beaverstone, and N. K. Nikolova, "Study of practical limitations of real-time microwave imaging of tissue," in *Proc. IEEE Int. Symp. Antennas Propag.*, San Diego, CA, USA, Jul. 2017.
- [32] Keysight (Agilent) Technologies, "Dielectric Probe Kit 200 MHz to 50 GHz, (85070E)," USA, 2014.
- [33] P. M. Meaney *et al.*, "Initial clinical experience with microwave breast imaging in women with normal mammography," *Acad. Radiol.*, vol. 14, no. 2, pp. 207–218, 2007.
- [34] M. Lazebnik *et al.*, "A large-scale study of the ultrawideband microwave dielectric properties of normal, benign and malignant breast tissues obtained from cancer surgeries," *Phys. Med. Biol.*, vol. 50, no. 20, pp. 6093–6115, Oct. 2007.
- [35] R. K. Amineh, A. Trehan, and N. K. Nikolova, "TEM horn antenna for ultra-wide band microwave breast imaging," *Prog. Electromagn. Res. B.*, vol. 13, pp. 59–74, 2009.
- [36] Mini-Circuits, "Coaxial High Power Amplifier (ZVE-3W-83+)," USA.
- [37] Mini-Circuits, "Low Noise, Wideband, High IP3 Monolithic Amplifier (PMA3-83LN+)," USA.
- [38] A. S. Beaverstone, "An electronically-switched sensor array for microwave imaging," M.A.Sc. thesis, McMaster Univ., Hamilton, ON, Canada, 2015.
- [39] A. S. Beaverstone and N. K. Nikolova, "Modeling and design of a switched transceiver array for tissue imaging," in *Proc. Numer. Electromagn. Multiphys. Model. Optim.*, Ottawa, ON, Canada, Aug. 2015, pp. 1–3.
- [40] F. Foroutan and N. K. Nikolova, "Dynamic range of an active radio sensor for bias-switched arrays for microwave tissue imaging," in *Proc. IEEE AP-S/URSI Int. Symp. Antennas Propag.*, Boston, MA, USA, Jul. 2018, Accepted.
- [41] D. Tajik, A. D. Pitcher, D. S. Shumakov, N. K. Nikolova, and J. W. Bandler, "Enhancing quantitative microwave holography in tissue imaging," in *Proc. Eur. Conf. Antennas Propag.*, London, U.K., Presented Apr. 2018.
- [42] The MathWorks, Inc., "MATLAB 2016a," USA, 2016.
- [43] Health Canada, "Guidelines on Exposure to Electromagnetic Fields from Magnetic Resonance Clinical Systems – Safety Code 26," Health Canada, Ottawa, ON, Canada, 1987.
- [44] Health Canada, "Limits of Human Exposure to Radiofrequency Electromagnetic Energy in the Frequency Range from 3 kHz to 300 GHz: Safety Code 6," Health Canada, Ottawa, ON, Canada, 2015.
- [45] A. Santorelli, M. V. Schueren, and M. Popovic, "SAR levels in microwave breast imaging: 3-D safety assessment with plane-wave illumination," in *Proc. Asia Pac. Microw. Conf.*, Melbourne, VIC, Australia, 2011, pp. 481–484.



Daniel Tajik received the Bachelor's degree in electrical and biomedical engineering and the Master's degree in electrical and computer engineering from McMaster University, Hamilton, ON, Canada, in 2015 and 2017, respectively. His Ph.D. research is focused on developing microwave image processing algorithms for use in medical diagnostics. His research interests include applications of microwave engineering in breast-cancer imaging, stroke detection, concealed weapon detection, and through-the-wall imaging, as well as antenna design for satellite communications. In 2017, he was the recipient of both the First Place and Audience Choice Awards in the first ever 3MT competition at the IEEE International Microwave Symposium for his presentation "Microwave Holography: The Future of Medical Imaging."



Farzad Foroutan received the Bachelor's degree in electrical engineering of telecommunication from Shahid Beheshti University, Tehran, Iran, in 2016. He is currently working toward the Master's degree at McMaster University, Hamilton, ON, Canada. His research lies in developing hardware for microwave imaging of the breast with a focus on designing active sensors for bias-switched arrays. His research interests include antenna design and microwave imaging methods for breast and brain cancer detection.



Denys S. Shumakov received the Master's degree in radio engineering from the National Technical University of Ukraine, Kiev, Ukraine, in 2010 and the Ph.D. degree in electrical engineering from McMaster University, Hamilton, ON, Canada, in 2017. From 2009 to 2013, he was the Medical Engineer with Materialise NV, which is a company offering 3-D printing software and services in healthcare. He is the author of ten journal articles and a book chapter. He is currently a Regulatory Policy and Risk Management Officer with Health Canada. From 2017 to

2018, he was the recipient of Canadian Science Policy Fellowship. From 2014 to 2017, he was the recipient of the McMaster International Excellence Award. He is a Reviewer for the IEEE TRANSACTIONS ON BIOMEDICAL ENGINEERING and the IEEE TRANSACTIONS ON MICROWAVE THEORY AND TECHNIQUES.



Aaron D. Pitcher received the Bachelor's of Engineering (with distinction) degree in electrical engineering program from McMaster University, Hamilton, ON, Canada, in 2016. He is currently working toward the M.A.Sc. degree at McMaster University, expecting graduation in November 2018. He specializes in the development of an ultra-wideband pulsed radar systems for microwave imaging and detection. His research interests include the application of microwaves in security and personnel protection systems, imaging diagnostics, and space communication.



Natalia K. Nikolova (S'93-M'97-SM'05-F'11) received the Dipl.Eng. degree from the Technical University of Varna, Varna, Bulgaria, in 1989 and the Ph.D. degree from the University of Electro-Communications, Tokyo, Japan, in 1997. From 1998 to 1999, she held a Postdoctoral Fellowship of the Natural Sciences and Engineering Research Council of Canada (NSERC), during which she was initially with the Microwave and Electromagnetics Laboratory, DalTech, Dalhousie University, Halifax, NS, Canada, and, later, for a year with the Simulation Optimization Systems Research Laboratory, McMaster University, Hamilton, ON, Canada.

In July 1999, she joined the Department of Electrical and Computer Engineering, McMaster University, where she is currently a Professor. Her research interests include inverse scattering and microwave imaging, theoretical and computational electromagnetism, as well as high-frequency computer-aided design. From 2000 to 2005, she was the recipient of a University Faculty Award of NSERC. Since 2008, she has been a Canada Research Chair in High-frequency Electromagnetics. She is a Fellow of the Canadian Academy of Engineering. From 2010 to 2013, she was a Distinguished Microwave Lecturer. She currently serves on three IEEE Technical Coordinating Committees: MTT-1 (Computer-aided Design), MTT-10 (Biological Effects and Medical Applications), and MTT-15 (Microwave Field Theory).